

# ***Engineering Topological Phases with a Traveling-Wave Spacetime Modulation***

*João C. Serra<sup>1</sup>, Mário G. Silveirinha<sup>2</sup>*

*University of Lisbon–Instituto Superior Técnico and Instituto de Telecomunicações,  
Avenida Rovisco Pais, 1, 1049-001 Lisboa, Portugal*

## **Abstract**

Time-variant systems have recently garnered considerable attention due to their unique potentials in manipulating electromagnetic waves. Here, we introduce a novel class of topological systems that rely on spacetime crystals with a traveling-wave modulation that emulates certain aspects of physical motion. Challenging intuition, our findings reveal that, even though such systems rely on a linear momentum bias, it is feasible to engineer an internal angular momentum and non-trivial topological phases by leveraging the symmetry of its structural elements. Furthermore, we establish that the proposed platforms exhibit a gauge degree of freedom associated with the arbitrariness in the choice of the coordinate transformation that eliminates the time dependence of the system's Hamiltonian. The system's topology is intricately governed by a synthetic magnetic potential whose field lines can be controlled by manipulating material anisotropy. Remarkably, we demonstrate that the proposed spacetime crystals host an unconventional class of scattering-immune edge states. The oscillation frequency of the edge states adapts continuously along the propagation path, shaped by the geometric attributes of the path itself.

---

<sup>1</sup> E-mail: [joao.serra@lx.it.pt](mailto:joao.serra@lx.it.pt)

<sup>2</sup> To whom correspondence should be addressed: [mario.silveirinha@tecnico.ulisboa.pt](mailto:mario.silveirinha@tecnico.ulisboa.pt)

## Main Text

Topological photonics provides an elegant theoretical framework to characterize the energy flow near the “boundaries” of material structures with complete band gaps [1-4]. Topological systems are usually engineered by modulating in space the material response. Recently, the crystal concept has been extended to structures presenting time modulations [5, 6, 7, 8, 9], opening up many interesting theoretical possibilities. Time and spacetime modulations enable exotic and nonreciprocal light-matter interactions without an external magnetic field bias, which can be useful for a myriad of optical applications [10, 11, 12].

Crystals with a (linear) spacetime traveling-wave modulation, e.g.,  $\varepsilon = \varepsilon(\mathbf{r} - \mathbf{v}t)$  with  $\mathbf{v}$  the modulation speed, are especially relevant as they enable a relatively simple analytical modelling and because they can be used to engineer a synthetic motion [13, 14, 15, 16]. Heuristically, one may expect that nontrivial topological Chern phases are associated with some form of internal angular momentum [18, 19]. For instance, the nontrivial topology of a magnetized plasma is deeply rooted in the angular momentum generated by the static magnetic bias through the electron cyclotron orbits [20]. This property may suggest that linear spacetime modulations are unsuitable to generate nontrivial topological phases. In this Letter, we will show that counterintuitively such an understanding is wrong, and that one may engineer a synthetic angular momentum bias and nontrivial topological phases in crystals with a pure traveling-wave modulation. Our findings are not only interesting from a theoretical standpoint, but also unveil an exciting new route to engineer nontrivial material topologies in spacetime crystals. Different topological aspects of time-dependent systems have been previously discussed in the literature [21-27]. To our best knowledge, here we present the first strict (i.e., without resorting to an effective theory approximation) example of a spacetime crystal with a nontrivial Chern topology.

For simplicity, our analysis is focused on two-dimensional platforms invariant to translations along the  $z$ -direction and on propagation in the  $xoy$  plane ( $\partial_z \equiv \partial/\partial z = 0$ ). For such systems the transverse electric (TE,  $H_z = 0$ ) and the transverse magnetic (TM,  $E_z = 0$ ) polarizations are decoupled. Without loss of generality, here we consider only TE polarized waves. The TE-waves are fully described by the field components  $\Psi = (E_z \ H_x \ H_y)^T$ , which satisfy the Schrödinger-type equation:

$$\begin{pmatrix} 0 & -i\partial_y & +i\partial_x \\ -i\partial_y & 0 & 0 \\ +i\partial_x & 0 & 0 \end{pmatrix} \cdot \Psi(\mathbf{r}, t) = i \frac{\partial}{\partial t} [\mathbf{M}_{\text{TE}}(\mathbf{r}, t) \cdot \Psi(\mathbf{r}, t)], \quad \mathbf{M}_{\text{TE}}(\mathbf{r}, t) = \begin{pmatrix} \varepsilon_{zz} & 0 & 0 \\ 0 & \mu_{xx} & \mu_{xy} \\ 0 & \mu_{xy} & \mu_{yy} \end{pmatrix}. \quad (1)$$

Note that TE-waves only probe the  $zz$  component of the permittivity tensor and the in-plane components ( $xx$ ,  $xy$ ,  $yy$ ) components of the (symmetric) permeability tensor. It will be shown later that materials exhibiting anisotropic responses play a crucial role in creating topological phases. The material matrix  $\mathbf{M}_{\text{TE}}(\mathbf{r}, t)$  is supposed to have a traveling-wave type structure such that the space and time variations are synchronized as  $\mathbf{M}_{\text{TE}}(\mathbf{r}, t) = \mathbf{M}_{\text{TE}}(\mathbf{r} - \mathbf{v}t)$ , where  $\mathbf{v}$  is the modulation speed. This type of modulation shares some resemblances with moving systems [13, 14, 15, 16], albeit the two in general are not equivalent [17].

In order to characterize the spacetime crystal topology, we switch to a Lorentz co-moving frame where the material matrix  $\mathbf{M}'_{\text{TE}}$  becomes time independent. The electrodynamics in the co-moving frame (primed coordinates) is described by:

$$\mathbf{L}(-i\nabla') \cdot \Psi'(\mathbf{r}', t') = i\mathbf{M}'_{\text{TE}}(\mathbf{r}') \cdot \frac{\partial}{\partial t'} \Psi'(\mathbf{r}', t'), \quad \mathbf{M}'_{\text{TE}} = \begin{pmatrix} \varepsilon'_{zz} & \xi'_{zx} & \xi'_{zy} \\ \xi'_{zx} & \mu'_{xx} & \mu'_{xy} \\ \xi'_{zy} & \mu'_{xy} & \mu'_{yy} \end{pmatrix}. \quad (2)$$

The formulas for the transformed material parameters  $\varepsilon'_{zz}$ ,  $\mu'_{ij}$ ,  $\xi'_{z,i}$  ( $i, j = x, y$ ) are given in the supplementary information [28]. In the above,  $\Psi' = (E'_z \ H'_x \ H'_y)^T$  is the transformed

state vector written in terms of the fields in the co-moving frame. The operator  $\mathbf{L}(-i\nabla')$  is the differential operator on the left-hand side of Eq. (1) with  $\partial_x \rightarrow \partial_{x'}$  and  $\partial_y \rightarrow \partial_{y'}$ .

As usual, the Lorentz transformation creates a magneto-electric coupling in the material response [15, 17, 29], here described by the elements  $\xi'_{zx}$  and  $\xi'_{zy}$ . Importantly, the magneto-electric coupling coefficients are associated with a gauge degree of freedom. The gauge freedom is due to the arbitrariness in the choice of the coordinate transformation. In fact, there is a wide class of transformations that can be used to eliminate the time dependence of the material parameters, the simplest examples being the Lorentz and the Galilean transformations [17, 28]. All the studies in the main text rely on a standard Lorentz transformation. In the supplementary information, we show that the state vector associated with a generic coordinate transformation (e.g., a Galilean transformation) is related to the state vector associated with the Lorentz transformation through a gauge transformation of the type  $\Psi' \rightarrow \Psi' e^{ik_\Delta \cdot \mathbf{r}'}$  with  $\mathbf{k}_\Delta$  independent of the coordinates  $\mathbf{r}'$  [28]. Thus,  $\Psi'$  may be understood as a gauge field.

As already noted in previous works [27, 30, 31], there is a synthetic magnetic potential associated with the magneto-electric tensor. The dimensionless magnetic potential for TE waves is defined by  $\mathbf{A} = [c\xi'_{zx}\hat{\mathbf{x}} + c\xi'_{zy}\hat{\mathbf{y}}] \times \hat{\mathbf{z}}$  [30]. We show in the supplementary information that while  $\mathbf{A}$  depends on the gauge, i.e., it depends on the particular coordinate transformation, the corresponding synthetic magnetic field  $\nabla \times \mathbf{A}$  is gauge independent.

For isotropic materials ( $\varepsilon_{zz} \equiv \varepsilon$ ,  $\mu_{xx} = \mu_{yy} \equiv \mu$  and  $\mu_{xy} = 0$ ), the direction of the synthetic potential is strictly locked to the direction of the modulation speed as  $\mathbf{A} \approx -(n^2 - 1)\mathbf{v}/c$ . Here,  $n = c\sqrt{\varepsilon\mu}$  is the refractive index of the material, and for simplicity we ignore second order relativistic corrections [28]. The simplest and most intuitive way to create an internal

angular momentum is to engineer a magnetic potential  $\mathbf{A}$  with an azimuthal-type structure so that the vector field lines follow circular orbits. This solution was studied in our previous work [27] using an effective medium formalism and rotating spacetime modulations. The linear spacetime modulation is seemingly incompatible with such class of solutions, due to the aforementioned restriction on the direction of  $\mathbf{A}$ . This constraint supports the heuristic reasoning that a linear momentum bias is unsuitable to generate topological Chern phases.

To illustrate the difficulty in generating topological phases in the considered platform, we consider a spacetime crystal formed by cylindrical isotropic rods (Fig. 1a). Due to the Lorentz contraction, the geometry of the spacetime crystal is slightly different in the laboratory and co-moving frames [17]. Specifically, all the geometrical distances are contracted by the Lorentz factor  $\gamma = (1 - v^2 / c^2)^{-1/2}$  in the laboratory frame along the direction of  $\mathbf{v}$ . For simplicity, we fix the lattice structure (honeycomb lattice) and the geometrical shapes (circular rods) in the co-moving frame. Thereby, the rods have slightly ellipsoidal cross-sections in the laboratory frame coordinates. There are two inequivalent rods per unit cell (represented in red and green in Fig. 1a) with permittivities  $\varepsilon_1$  and  $\varepsilon_2$  and a trivial permeability in the laboratory frame. For simplicity, the background region is taken as air, so that its response is unaffected by the Lorentz transformation [17]. The band structure of a honeycomb lattice is characterized by Dirac cones at the high-symmetry points  $K$  and  $K'$  [32, 33, 34]. In most systems, breaking either the parity ( $\mathcal{P}$ ) or time-reversal ( $\mathcal{T}$ ) symmetries is sufficient to lift this degeneracy (the parity operator  $\mathcal{P} : (x, y) \rightarrow (-x, -y)$  represents a two-fold rotation). As time-varying systems have a broken  $\mathcal{T}$ -symmetry, the modulation of the material parameters can potentially open a topologically nontrivial gap. Figure 1b presents the band structure of the spacetime crystal in the Lorentz co-moving frame calculated using the plane wave expansion method for different modulation speeds along the

y-axis [28]. The rods are assumed identical ( $\varepsilon_1 = \varepsilon_2 = 12\varepsilon_0$ ). Surprisingly, the Dirac degeneracies are not lifted for  $v \neq 0$ . Instead, they are shifted in the momentum space  $(k'_x, k'_y)$  along the direction of  $\mathbf{v}$ . This result holds true for an arbitrary orientation and amplitude of  $\mathbf{v}$ . Importantly, even if the band gap could be opened, it would necessarily be topologically trivial. In fact, when  $\varepsilon(\mathbf{r}, t = 0) = \varepsilon(-\mathbf{r}, t = 0)$  the system is  $\mathcal{P} \cdot \mathcal{T}$  symmetric. Note that both the time-reversal and the parity operators flip the direction of the modulation speed, so that  $\mathbf{v}$  is unchanged under the composition of the two operators.  $\mathcal{P} \cdot \mathcal{T}$  symmetric systems have vanishing Berry curvature and thereby have always a trivial topology [28].

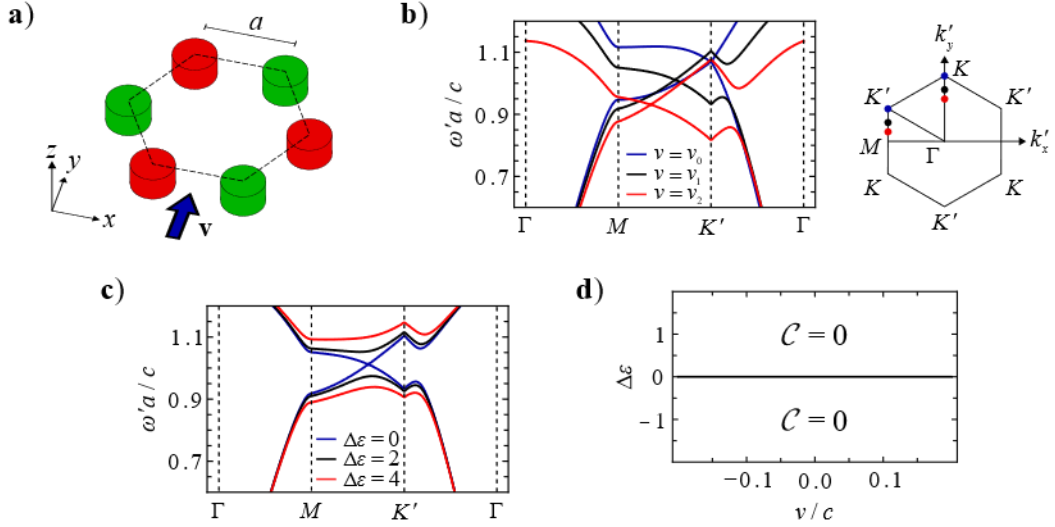


**Fig. 1** **a)** Unit cell of a spacetime crystal with modulation velocity  $\mathbf{v} = v\hat{\mathbf{y}}$ . The unit cell contains two dielectric inclusions with permittivity  $\varepsilon_1$  (red regions) and  $\varepsilon_2$  (green regions). In the Lorentz co-moving frame, the crystal has a honeycomb lattice and the inclusions have a circular cross-section with radius  $R = 0.3a$ , being  $a$  the nearest neighbors distance. In the laboratory frame, the crystal is Lorentz contracted. **b)** Band structure in the Lorentz co-moving frame of a crystal with identical inclusions ( $\varepsilon_1 = \varepsilon_2 = 12\varepsilon_0$ ) for different modulation speeds:  $v_0 = 0.0c$  (blue),  $v_1 = -0.1c$  (black),  $v_2 = -0.2c$  (red). The Dirac degeneracies are not lifted by the synthetic motion, their position is shifted in the Brillouin Zone along the direction of  $\mathbf{v}$  (right hand-side inset). **c)** Band structure in the Lorentz co-moving frame with a modulation speed  $v = -0.1c$  for inclusions with  $\varepsilon_1 = \left(12 + \frac{\Delta\varepsilon}{2}\right)\varepsilon_0$  and  $\varepsilon_2 = \left(12 - \frac{\Delta\varepsilon}{2}\right)\varepsilon_0$  for  $\Delta\varepsilon = 0$  (blue line),  $\Delta\varepsilon = 2$  (black line),  $\Delta\varepsilon = 4$  (red line). **d)**

Topological phase diagram for different values of the permittivity detuning  $\Delta\varepsilon$  and of the modulation speed  $v$ . If the  $\mathcal{P}\cdot\mathcal{T}$  symmetry is preserved ( $\Delta\varepsilon = 0$ ), the band gap remains closed; otherwise, a complete band gap is formed but with a trivial topology.

From the previous discussion, it is manifest that to create a nontrivial topology one needs to break the two-fold rotation (parity) symmetry of the static crystal, i.e., guarantee that  $\varepsilon(\mathbf{r}, t = 0) \neq \varepsilon(-\mathbf{r}, t = 0)$ . The simplest way to do this is to detune the permittivity of the two inclusions so that  $\varepsilon_{1,2} / \varepsilon_0 = 12 \pm \Delta\varepsilon / 2$ . As shown in Fig. 1c, a permittivity detuning  $\Delta\varepsilon \neq 0$  does indeed create a full gap in the co-moving frame band diagram. However, it turns out that the topological charge of the band gap is always trivial. The gap Chern number is numerically calculated using the Green's function method [35, 36, 37, 38] (see Ref. [28]). The vanishing topological charge is consistent with well known properties of the Haldane model, where the parity symmetry breaking always favours trivial topologies [39]. A general discussion on how symmetry constraints the formation of topological phases in spacetime crystals can be found in the supplementary information [28]. Figure 1d summarizes our findings in the form of a topological phase diagram. Note that the phase diagram is precisely the same for other spacetime coordinate transformations (e.g., for a Galilean transformation) because the eigenstates obtained with different gauges are related as  $\Psi' \rightarrow \Psi' e^{ik_\Delta \cdot r'}$ .

As previously mentioned, for isotropic spacetime crystals the direction of the synthetic vector potential is locked to the modulation speed as  $\mathbf{A} \approx -(n^2 - 1)\mathbf{v} / c$ . Interestingly, for an isorefractive crystal formed by isotropic materials with  $n = 1$  the vector potential vanishes exactly. In fact, materials with  $n = 1$  are “fixed points” of the Lorentz transformation, i.e., such media have the same constitutive relations in any inertial frame [17, 40, 42]. We refer to such class of materials as Minkowskian isorefractive media [17, 40, 41, 42]. Crystals formed

by Minkowskian isorefractive media have a trivial magneto-electric response in the Lorentz co-moving frame ( $\xi'_{zx} = \xi'_{zy} = 0$ ) and hence are always topologically trivial.

It is useful to analyze how the vector potential  $\mathbf{A}$  changes when the condition  $n = \text{const.}$  is slightly perturbed with a weak magnetic anisotropy. For conciseness in the main text, we restrict the discussion to the Minkowskian case ( $n=1$ ), but all the results can be readily extended to isorefractive crystals formed by isotropic materials with  $1 < n = \text{const.}$  [28]. To this end, we consider a spacetime crystal such that the in-plane permeability is of the form  $\mu \left[ (1 + \delta_\mu) \hat{\mathbf{e}}_1 \otimes \hat{\mathbf{e}}_1 + (1 - \delta_\mu) \hat{\mathbf{e}}_2 \otimes \hat{\mathbf{e}}_2 \right]$ . Here,  $\hat{\mathbf{e}}_1, \hat{\mathbf{e}}_2$  are the in-plane orthogonal permeability main axes, defined so that  $\hat{\mathbf{e}}_1 \times \hat{\mathbf{e}}_2 = \hat{\mathbf{z}}$ . The in-plane permeability eigenvalues are  $\mu(1 \pm \delta_\mu)$ . All the parameters ( $\hat{\mathbf{e}}_1, \hat{\mathbf{e}}_2, \mu, \delta_\mu$ ) are functions of  $\mathbf{r} - \mathbf{v}t$  in the laboratory frame coordinates. Furthermore, it is supposed that  $\varepsilon_{zz}\mu = 1/c^2$  so that when  $\delta_\mu = 0$  the crystal has a constant refractive index. Thus,  $\delta_\mu$  gives the detuning with respect to the isorefractive case. A straightforward analysis shows that the synthetic vector potential associated with such an anisotropic crystal is given by [28]:

$$\mathbf{A} = \frac{v}{c} \delta_\mu \hat{\mathbf{e}}_A, \quad \text{with} \quad \hat{\mathbf{e}}_A \equiv \cos(2\varphi_\mu - \varphi_v) \hat{\mathbf{x}} + \sin(2\varphi_\mu - \varphi_v) \hat{\mathbf{y}}. \quad (3)$$

As seen, the vector potential is proportional to both the velocity  $v$  and to the permeability detuning  $\delta_\mu$ , so that  $\mathbf{A}$  vanishes in the Minkowskian case ( $n=1$ ). In the above,  $\varphi_\mu$  ( $\varphi_v$ ) represents the angle of the main axis  $\hat{\mathbf{e}}_1$  (modulation speed  $\mathbf{v}$ ) with respect to the  $x$ -direction (Fig. 2a). Remarkably, the direction of the vector potential is not locked to the modulation speed, but depends as well on the axes of the permeability tensor. In particular, by changing continuously the direction ( $\varphi_\mu$ ) of  $\hat{\mathbf{e}}_1$  it is possible to engineer a vector potential with an arbitrary orientation! This property is geometrically illustrated in Fig. 2a. As seen, the



direction of  $\mathbf{A}$  is obtained by rotating the vector  $\mathbf{v}$  by an angle of  $\Delta\varphi = 2(\varphi_\mu - \varphi_v)$  with respect to the  $z$ -axis.

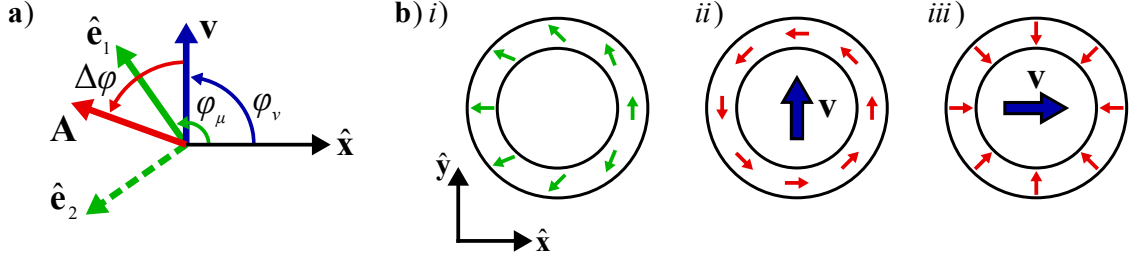


**Fig. 2 a)** Geometrical relation between the modulation velocity (blue), the permeability main axes (green) and the synthetic magnetic potential (red). The orientation of the modulation velocity and the magnetic potential differ by the angle  $\Delta\varphi = 2(\varphi_\mu - \varphi_v)$ . The material response is a slight anisotropic perturbation of a Minkowskian isotropic medium. **bi)** Geometry of an anisotropic ring such that the permeability main axes rotate continuously by a half-turn along its perimeter. The direction of the main axis  $\hat{\mathbf{e}}_1$  is represented by the green arrows. The synthetic magnetic potential  $\mathbf{A}$  field lines are represented by the red arrows for  $\mathbf{v} = v\hat{\mathbf{y}}$  in (bii) and for  $\mathbf{v} = v\hat{\mathbf{x}}$  in (biii). The synthetic motion induces an internal angular momentum only in ii).

Motivated by this result, we introduce an anisotropic ring (Fig. 2bi) that effectively behaves as a rotating ring when subject to a linear modulation with  $\mathbf{v} = v\hat{\mathbf{y}}$ . The ring is formed by an anisotropic material with the main axis  $\hat{\mathbf{e}}_1$  of the permeability tensor (green arrows) varying continuously along the ring perimeter such that  $\varphi_\mu = \pi/2 + \varphi/2$  with  $\varphi$  the polar angle measured with respect to the ring centre. Note that in a full cycle  $\hat{\mathbf{e}}_1$  is transformed into  $-\hat{\mathbf{e}}_1$ , but the permeability tensor is transformed as  $\boldsymbol{\mu} \rightarrow +\boldsymbol{\mu}$  because it is insensitive to the “polarity” of  $\hat{\mathbf{e}}_1$ . This property is reminiscent of the “fermionic half-turn” periodicity of the polarization vector in a conical diffraction ring [43]. Figures 2bii and 2biii show the vector field lines of the synthetic magnetic potential [Eq. (3)] when the modulation speed is directed along the  $y$  and  $x$  directions, respectively. Remarkably, for  $\mathbf{v} = v\hat{\mathbf{y}}$  the  $\mathbf{A}$  lines are azimuthal whereas for  $\mathbf{v} = v\hat{\mathbf{x}}$  they are radial. A spacetime crystal formed by many

of such rings (see below) has a nontrivial internal angular momentum (heuristically defined as  $\mathcal{L} \sim \int ds' \hat{\mathbf{z}} \cdot (\mathbf{r}' \times \mathbf{A})$ ) and a nontrivial topology only when  $\mathbf{v} = v\hat{\mathbf{y}}$ . In fact, as further discussed in the supplementary information [28], a spacetime crystal with a mirror plane parallel to the modulation velocity is necessarily topologically trivial. Note that the anisotropic ring has a mirror plane at  $y=0$  and so  $\mathbf{v} = v\hat{\mathbf{x}}$  leads to a trivial topology. It is also relevant to point out that the ring has broken two-fold rotation symmetry. Gauge fields relying on anisotropic materials were previously discussed in a different context [44].

Figure 3a depicts a spacetime crystal constructed from an isorefractive system (elements in red plus the background region) perturbed with a discrete version of the anisotropic ring (elements in gray). The elements in red and the background have refractive index  $n=1$  (Minkowskian crystal). Thereby, the synthetic magnetic potential is generated exclusively by the elements in the center. The role of the red elements is to engineer band degeneracies at the Dirac points that are lifted by the spacetime modulation.

The 3 elements in gray are placed along the perimeter of a circle with radius  $R = 0.35a$  at the azimuth angles  $\varphi_n = -\frac{\pi}{2} + (n-1)\frac{2\pi}{N}$  with  $n=1, \dots, N$  and  $N=3$ . The scatterers are formed by an anisotropic material with  $\delta_\mu = 0.5$ , with the main axis  $\hat{\mathbf{e}}_1$  of the permeability tensor directed along  $\varphi_{\mu,n} = \frac{\pi}{2} + \frac{\varphi_n}{2}$ . The generated synthetic magnetic potential is shown in Fig. 3a.

Figure 3b depicts the band structure in the Lorentz co-moving frame for  $v=0.2c$ . The band gap shaded in blue is characterized by  $\mathcal{C}_{\text{gap}} = -1$ , in agreement with the azimuthal-type magnetic potential field lines in Fig. 3a. The corresponding Berry curvature is mostly concentrated at the two Dirac points [28]. In the supplementary materials, we present a detailed convergence study of the gap Chern number.

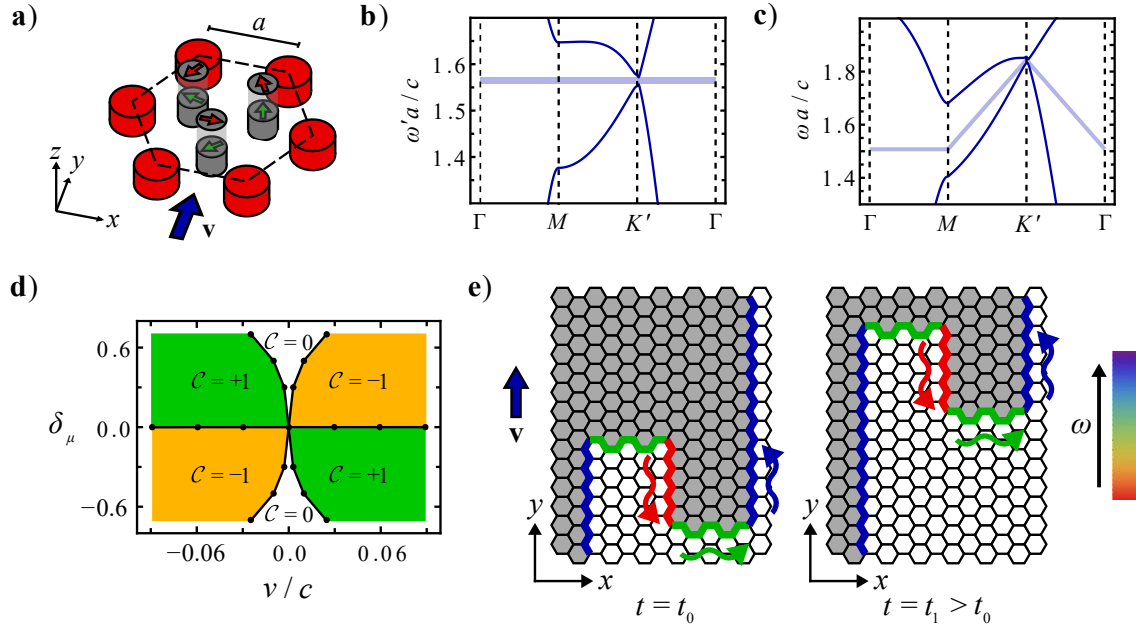


**Fig. 3** **a)** Unit cell of a spacetime crystal constructed from an isorefractive system (air background plus the honeycomb array of isotropic red elements with  $\varepsilon=10\varepsilon_0$  and  $\mu=0.1\mu_0$ ) perturbed with the gray anisotropic elements. The gray elements provide a discrete realization of the anisotropic ring (Fig. 2bi). They have an anisotropic response characterized by the detuning parameter  $\delta_\mu=0.5$  and the permeability main axis  $\hat{\mathbf{e}}_1$  is represented by the green arrows. We represent the corresponding synthetic magnetic potential  $\mathbf{A}$  in the Lorentz co-moving frame with the red arrows above the cylinders. The red and gray elements have circular cross-sections with radii  $R_r=0.2a$  and  $R_g=0.17a$ , respectively. All the dimensions are specified in the Lorentz co-moving frame. **b)** Band structure in the Lorentz co-moving frame for a modulation speed  $v=0.2c$  along the y-direction. The band gap is characterized by  $\mathcal{C}_{\text{gap}}=-1$ . **c)** Band structure in the laboratory frame. **d)** Topological phase diagram as a function of the modulation speed  $v$  and of the detuning parameter  $\delta_\mu$ . **e)** Time evolution of the interface between two topologically inequivalent spacetime crystals (shaded in gray and in white colors), as seen in the lab frame. Both crystals are subject to the same modulation speed  $\mathbf{v}$  along the y-direction. It is supposed that the interface supports a single unidirectional edge state. Due to the synthetic Doppler shift, the frequency observed in the lab frame changes with the direction of propagation of the edge state (see the color bar).

The band structure in the laboratory frame can be found from the band structure in the co-moving frame using a relativistic Doppler transformation  $k_x=k'_x$ ,  $k_y=\gamma(k'_y+\omega'v/c^2)$  and

$\omega = \gamma(\omega' + vk'_y)$  [17, 45]. As shown in Fig. 3c, due to the Doppler shift, the band structure exhibits a slant long the  $k_y$  direction in the laboratory frame coordinates. Consequently, the band gap is no longer a horizontal strip in the  $(\mathbf{k}, \omega)$ -space, but rather a slanted strip. Figure 3d shows the topological phase diagram in terms of the modulation speed  $v$  and the detuning parameter  $\delta_\mu$ . Similar to the synthetic vector potential [Eq. (3)], the gap Chern number changes sign when either  $v$  or  $\delta_\mu$  change sign. There are two regions of the parametric space where the system remains topologically trivial. Specifically, a nontrivial topology is feasible only when  $v$  is larger than some threshold value that depends on  $\delta_\mu$ . In the supplementary materials, we present a study of other implementations of the anisotropic ring with a different number  $N$  of scatterers [28]. It is shown that a ring with a larger number of elements provides more robust topological phases. Furthermore, we also prove that it is possible to engineer nontrivial topologies using only isotropic materials [28].

A nontrivial topological phase is associated with the propagation of unidirectional edge modes. In the laboratory frame, the edge modes are immune to back-scattering but rather peculiarly their frequency of oscillation may change along the propagation path due to the synthetic Doppler shift. For an edge mode propagating along the direction  $\hat{\mathbf{t}}'$  (tangent to the boundary wall), its frequency as observed in the laboratory frame is  $\omega = \gamma(\omega' + vk'_{\text{egde}} \hat{\mathbf{t}}' \cdot \mathbf{v})$ . Here,  $\omega'$  and  $k'_{\text{egde}}$  are the frequency and propagation constant of the edge mode in the co-moving frame coordinates. Note that  $k'_{\text{egde}}$  may depend on  $\hat{\mathbf{t}}'$ , but  $\omega'$  is independent of the propagation path. As the interface between two topologically inequivalent spacetime crystals undergoes deformation, the frequency of the primary oscillation continuously shifts, as sketched in Fig. 3e. This property introduces a unique concept: the potential for a wave to travel along a spacetime interface without any form of back-scattering, all while its frequency

experiences continuous variation along the propagation path. This distinctive trait opens up intriguing possibilities for employing topological spacetime crystals in frequency-conversion applications, while entirely avoiding any type of back-scattering interference.

In summary, we introduced a novel class of topological systems relying on spacetime traveling-wave modulations. We have demonstrated that, despite the linear momentum bias inherent in such systems, it is indeed possible to engineer an internal angular momentum and harness topological phases by leveraging the anisotropy of the materials. Notably, we have established that spacetime crystals possess a gauge degree of freedom tied to the selection of the coordinate transformation that eliminates the time dependence of the material response. The system topology is dictated by a gauge-dependent synthetic magnetic field whose orientation can be controlled by tailoring the main axes of the material tensors. The introduced systems open up an exciting new paradigm for light transport that defies back-scattering with the frequency of edge modes controlled by the shape of the spacetime boundary. Our findings pave the way for applications in the manipulation of light frequencies, showcasing the remarkable potential of these innovative structures.

**Acknowledgements:** This work is supported in part by the Institution of Engineering and Technology (IET), by the Simons Foundation Award 733700, and by Fundação para a Ciência e a Tecnologia and Instituto de Telecomunicações under Project No. UIDB/50008/2020.

## References:

- [1] L. Lu, J. D. Joannopoulos, M. Soljačić, “Topological photonics”, *Nat. Photonics* **8**, 821 (2014).
- [2] Z. Wang, Y. Chong, J. D. Joannopoulos, M. Soljačić, “Observation of unidirectional backscattering immune topological electromagnetic states”, *Nature (London)* **461**, 772 (2009).
- [3] T. Ozawa, H. M. Price, A. Amo, N. Goldman, M. Hafezi, L. Lu, M. C. Rechtsman, D. Schuster, J. Simon, O. Zilberberg *et al*, “Topological photonics”, *Rev. Mod. Phys.* **91**, 015006 (2019).
- [4] M. G. Silveirinha, “Geometry and Topological Photonics”, *J. Optics*, **25**, 085102, (2023).
- [5] E. Galiffi, R. Tirole, S. Yin, H. Li, S. Vezzoli, P. A. Huidobro, M. G. Silveirinha, R. Sapienza, A. Alù, J. B. Pendry, “Photonics of time-varying media”, *Adv. Photonics* **4**, 014002 (2022).
- [6] Z.-L. Deck-Léger, N. Chamanara, M. Skorobogatiy, M. G. Silveirinha, C. Caloz, “Uniform-velocity spacetime crystals”, *Adv. Photon.* **1** (5), 056002 (2019).

- [7] C. Caloz, Z.-L. Decker-Léger, A. Bahrami, O. C. Vicente, Z. Li, “Generalized Space-Time Engineered Modulation (GSTEM) Metamaterials: A global and extended perspective”, *IEEE Antennas and Propagation Magazine*, DOI: 10.1109/MAP.2022.3216773 (2022).
- [8] N. Engheta, “Metamaterials with high degrees of freedom: Space, time, and more”, *Nanophotonics* **10**, 639 (2021).
- [9] V. Pacheco-Peña, N. Engheta, “Temporal aiming”, *Light: Science & Applications* **9**, 129 (2020).
- [10] D. L. Sounas, A. Alù, “Angular-Momentum-Biased Nanorings To Realize Magnetic-Free Integrated Optical Isolation”, *ACS Photonics* **1**, 3 (2014).
- [11] N. A. Estep, D. L. Sounas, J. Soric, A. Alù, “Magnetic-free non-reciprocity and isolation based on parametrically modulated coupled-resonator loops”, *Nat. Phys.* **10**, 923 (2014).
- [12] D. L. Sounas, A. Alù, “Non-reciprocal photonics based on time modulation”, *Nat. Photonics* **11**, 774 (2017).
- [13] Y. Mazor and A. Alù, “One-way hyperbolic metasurfaces based on synthetic motion”, *IEEE Trans. Antennas Propag.*, **68**, 1739 (2020).
- [14] P. A. Huidobro, E. Galiffi, S. Guenneau, R. V. Craster and J. B. Pendry, “Fresnel drag in space-time-modulated metamaterials,” *Proc. Natl. Acad. Sci. USA* **116**, 24943 (2019).
- [15] P. A. Huidobro, M. G. Silveirinha, E. Galiffi, J. B. Pendry, “Homogenization Theory of Space-Time Metamaterials”, *Phys. Rev. Appl.* **16**, 014044 (2021).
- [16] F. R. Prudêncio, M. G. Silveirinha, “Synthetic Axion Response with Spacetime Crystals”, *Phys. Rev. Appl.*, **19**, 024031, (2023).
- [17] F. R. Prudêncio, M. G. Silveirinha, “Replicating Physical Motion with Minkowskian Isorefractive Spacetime Crystals”, *Nanophotonics*, doi.org/10.1515/nanoph-2023-0144 (2023).
- [18] M. G. Silveirinha, “Quantized angular momentum in topological optical systems”, *Nat. Commun.* **10**, 349 (2019).
- [19] M. G. Silveirinha, “Proof of the Bulk-Edge Correspondence through a Link between Topological Photonics and Fluctuation-Electrodynamics”, *Phys. Rev. X* **9**, 011037 (2019).
- [20] M. G. Silveirinha, “Topological Angular Momentum and Radiative Heat Transport in Closed Orbits”, *Phys. Rev. B*, **95**, 115103, (2017).
- [21] M. Hafezi, E. Demler, M. Lukin, J. Taylor, “Robust optical delay lines with topological protection”, *Nat. Phys.* **7**, 907 (2011).
- [22] K. Fang, Z. Yu, S. Fan, “Realizing effective magnetic field for photons by controlling the phase of dynamic modulation”, *Nat. Photonics* **6**, 11 (2012).
- [23] R. Fleury, A. B. Khanikaev, A. Alù, “Floquet topological insulators for sound”, *Nat. Comm.* **7**, 11744 (2016).
- [24] M. S. Rudner, N. H. Lindner, E. Berg, M. Levin, “Anomalous Edge States and the Bulk-Edge Correspondence for Periodically Driven Two-Dimensional Systems”, *Phys. Rev. X* **3**, 031005 (2013).
- [25] E. Lustig, Y. Sharabi, M. Segev, “Topological aspects of photonic time crystals”, *Optica* **5**, 1390 (2018).
- [26] L. Yuan, Q. Lin, M. Xiao, S. Fan, “Synthetic dimension in photonics”, *Optica* **5**, 11 (2018).
- [27] J. C. Serra, M. G. Silveirinha, “Rotating spacetime modulation: Topological phases and spacetime Haldane model”, *Phys. Rev. B* **107**, 035133 (2023).

- [28] Supplementary online information with additional discussion on A) Generalized Lorentz transformations, B) gauge transformations, C) the synthetic magnetic potential, D) the numerical calculation of the band structure of the spacetime crystal, E) the numerical calculation of the gap Chern number, F) symmetry constraints on the emergence of unidirectional edge modes, G) spacetime crystals with a square lattice, H) other implementations of the “anisotropic ring”.
- [29] J. A. Kong, *Electromagnetic Wave Theory* (New York: Wiley-Interscience), (1990).
- [30] S. Lannebère, M. G. Silveirinha, “Photonic analogues of the Haldane and Kane-Mele models”, *Nanophotonics* **8**, 1387 (2019).
- [31] F. R. Prudêncio, M. G. Silveirinha, “First principles calculation of the topological phases of the photonic Haldane model”, *Symmetry* **13**, 2229 (2021).
- [32] J. von Neumann, E. Wigner, “On the behaviour of eigenvalues in adiabatic processes”, *Physik Z.* **30**, 467 (1929).
- [33] J.-M. Hou, W. Chen, “Hidden symmetry and protection of Dirac points on the honeycomb lattice”, *Sci. Rep.* **5**, 17571 (2015).
- [34] W.-Y. He, C. T. Chan, “The Emergence of Dirac points in Photonic Crystals with Mirror Symmetry”, *Sci. Rep.* **5**, 8186 (2015).
- [35] M. G. Silveirinha, “Topological classification of Chern-type insulators by means of the photonic Green function”, *Phys. Rev. B*, **97**, 115146, (2018).
- [36] M. G. Silveirinha, “Topological theory of non-Hermitian photonic systems”, *Phys. Rev. B* **99**, 125155 (2019).
- [37] F. R. Prudêncio, M. G. Silveirinha, “First principles calculation of topological invariants of non-Hermitian photonic crystals”, *Commun. Phys.* **3**, 221 (2020).
- [38] F. R. Prudêncio, M. G. Silveirinha, “Ill-defined topologies in local dispersive photonic systems”, *Phys. Rev. Lett.*, **129**, 133903, (2022).
- [39] F. D. M. Haldane, “Model for a quantum Hall effect without Landau levels: condensed-matter realization of the «parity anomaly»”, *Phys. Rev. Lett.* **61**, 2015 (1988).
- [40] C. R. Paiva and S. A. Matos, “Minkowskian isotropic media and the perfect electromagnetic conductor,” *IEEE Trans. Antennas Propag.*, **60**, 3231, (2012).
- [41] J. B. Pendry, P. A. Huidobro, M. G. Silveirinha, E. Galiffi, “Crossing the light line”, *Nanophotonics*, **11**, 161, 2022.
- [42] A. Alex-Amor, C. Molero, M. G. Silveirinha, “Analysis of Metallic Spacetime Gratings using Lorentz Transformations”, *Phys. Rev. Appl.*, **20**, 014063, (2023).
- [43] M.V. Berry, M.R. Jeffrey, “Conical diffraction: Hamilton’s diabolical point at the heart of crystal optics”, Chapter 2, *Progress in Optics* (edited by E. Wolf,) **50**, (2007). (Elsevier).
- [44] F. Liu and J. Li, “Gauge Field Optics with Anisotropic Media”, *Phys. Rev. Lett.* **114**, 103902, (2015).
- [45] J. D. Jackson, *Classical Electrodynamics* (John Wiley & Sons, Inc., NY, 1999).

## Supplemental Information:

### *“Engineering Topological Phases with a Traveling-Wave Spacetime Modulation”*

*João C. Serra<sup>‡</sup>, Mário G. Silveirinha<sup>§</sup>*

University of Lisbon–Instituto Superior Técnico and Instituto de Telecomunicações, Avenida Rovisco Pais, 1, 1049-001 Lisboa, Portugal

The supplemental information provides additional details on A) generalized Lorentz transformations, B) gauge transformations, C) the synthetic magnetic potential, D) the numerical calculation of the band structure of the spacetime crystal, E) the numerical calculation of the gap Chern number, F) symmetry constraints on the emergence of unidirectional edge modes, G) spacetime crystals with a square lattice, H) other implementations of the “anisotropic ring”.

#### *A. Generalized Lorentz transformations*

In this supplementary note, we discuss how the material response changes under a generalized Lorentz transformation. Consider a linear time-variant material described by the laboratory frame constitutive relations

$$\begin{pmatrix} \mathbf{D}(\mathbf{r}, t) \\ \mathbf{B}(\mathbf{r}, t) \end{pmatrix} = \underbrace{\begin{pmatrix} \boldsymbol{\varepsilon}(\mathbf{r} - \mathbf{v}t) & \mathbf{0}_{3 \times 3} \\ \mathbf{0}_{3 \times 3} & \boldsymbol{\mu}(\mathbf{r} - \mathbf{v}t) \end{pmatrix}}_{\mathbf{M}} \begin{pmatrix} \mathbf{E}(\mathbf{r}, t) \\ \mathbf{H}(\mathbf{r}, t) \end{pmatrix}, \quad (\text{S1})$$

---

<sup>‡</sup> E-mail: [joao.serra@lx.it.pt](mailto:joao.serra@lx.it.pt)

<sup>§</sup> To whom correspondence should be addressed: [mario.silveirinha@tecnico.ulisboa.pt](mailto:mario.silveirinha@tecnico.ulisboa.pt)



with  $\boldsymbol{\varepsilon}$  and  $\boldsymbol{\mu}$  symmetric tensors. We introduce the generalized Lorentz transformation of coordinates [S1, S2]:

$$\mathbf{r}' = (\mathbf{1}_{\perp} + \gamma \hat{\mathbf{u}}_{\parallel} \otimes \hat{\mathbf{u}}_{\parallel}) \cdot \mathbf{r} - \gamma \mathbf{v} t, \quad t' = \gamma \left( t - \frac{\mathbf{v}}{c_0^2} \cdot \mathbf{r} \right) \quad (\text{S2})$$

Here,  $\mathbf{v} = v \hat{\mathbf{u}}_{\parallel}$ ,  $\mathbf{1}_{\perp} = \mathbf{1}_{3 \times 3} - \hat{\mathbf{u}}_{\parallel} \otimes \hat{\mathbf{u}}_{\parallel}$  and  $\gamma = 1 / \sqrt{1 - (v/c_0)^2}$ . For a regular Lorentz transformation,  $c_0 = c$  is the speed of light in vacuum. In some situations, it is useful to consider other generalized Lorentz transformations with  $0 < c_0 \leq \infty$  (see Ref. [S2]). For example, the case  $c_0 = \infty$  corresponds to a Galilean transformation of coordinates which is widely used to characterize the electromagnetic response of spacetime crystals with a traveling-wave modulation [S1, S2, S3]. Thus, there is a wide family of transformations that can be used to eliminate the time dependence of the material response. As further discussed in the supplementary note B, this arbitrariness in the choice of the coordinate transformation can be regarded as a gauge degree of freedom.

Following Refs. [S1, S2], the transformed electromagnetic fields are linked in the new coordinates as

$$\begin{pmatrix} \mathbf{D}'(\mathbf{r}', t') \\ \mathbf{B}'(\mathbf{r}', t') \end{pmatrix} = \mathbf{M}' \cdot \begin{pmatrix} \mathbf{E}'(\mathbf{r}', t') \\ \mathbf{H}'(\mathbf{r}', t') \end{pmatrix} \quad (\text{S3})$$

with  $\mathbf{M}'$  the transformed (time-independent) 6x6 material matrix given by:

$$\mathbf{M}' = \left[ \frac{1}{c_0^2} \mathbf{V} + \mathbf{A} \cdot \mathbf{M} \right] \cdot [\mathbf{A} + \mathbf{V} \cdot \mathbf{M}]^{-1}, \quad \text{with} \quad (\text{S4a})$$

$$\mathbf{V} = \begin{pmatrix} 0 & \gamma \mathbf{v} \times \mathbf{1} \\ -\gamma \mathbf{v} \times \mathbf{1} & 0 \end{pmatrix}, \quad \mathbf{A} = \begin{pmatrix} \gamma \mathbf{1}_{\perp} + \hat{\mathbf{u}}_{\parallel} \otimes \hat{\mathbf{u}}_{\parallel} & 0 \\ 0 & \gamma \mathbf{1}_{\perp} + \hat{\mathbf{u}}_{\parallel} \otimes \hat{\mathbf{u}}_{\parallel} \end{pmatrix}. \quad (\text{S4b})$$

The exact definition of the transformed fields can be found in Ref. [S2]. The transformed fields satisfy Maxwell's equations:

$$\begin{pmatrix} 0 & i\nabla' \times \mathbf{1} \\ -i\nabla' \times \mathbf{1} & 0 \end{pmatrix} \cdot \begin{pmatrix} \mathbf{E}'(\mathbf{r}', t') \\ \mathbf{H}'(\mathbf{r}', t') \end{pmatrix} = i \frac{\partial}{\partial t'} \mathbf{M}' \cdot \begin{pmatrix} \mathbf{E}'(\mathbf{r}', t') \\ \mathbf{H}'(\mathbf{r}', t') \end{pmatrix}. \quad (\text{S5})$$

It is convenient to write the transformed material matrix as:

$$\mathbf{M}' = \begin{pmatrix} \boldsymbol{\varepsilon}' & \boldsymbol{\xi}' \\ \boldsymbol{\zeta}' & \boldsymbol{\mu}' \end{pmatrix}, \quad (\text{S6})$$

where  $\boldsymbol{\varepsilon}'$  is the permittivity,  $\boldsymbol{\mu}'$  is the permeability and  $\boldsymbol{\xi}'$ ,  $\boldsymbol{\zeta}'$  are the magneto-electric tensors in the co-moving frame coordinates.

Let us consider now a scenario where the permittivity and permeability tensors are of the form:

$$\boldsymbol{\varepsilon} = \begin{pmatrix} \varepsilon_{xx} & \varepsilon_{xy} & 0 \\ \varepsilon_{xy} & \varepsilon_{yy} & 0 \\ 0 & 0 & \varepsilon_{zz} \end{pmatrix}, \quad \boldsymbol{\mu} = \begin{pmatrix} \mu_{xx} & \mu_{xy} & 0 \\ \mu_{xy} & \mu_{yy} & 0 \\ 0 & 0 & \mu_{zz} \end{pmatrix}, \quad (\text{S7})$$

So that the TE and TM polarizations can be decoupled into two sets of independent equations. Then, it can be easily checked that Maxwell's equations [Eq. (S5)] for TE-waves reduce to Eq. (2) of the main text. The elements  $\varepsilon'_{zz}$ ,  $\mu'_{xx}$ ,  $\mu'_{yy}$ ,  $\mu'_{xy}$ ,  $\xi'_{zx}$ ,  $\xi'_{zy}$  can be found by inserting Eq. (S7) into Eqs. (S4) and (S6), as detailed in the following subsections.

### *I. Non-relativistic limit*

Let us first ignore the relativistic corrections, i.e., consider a first order Taylor expansion of  $\mathbf{M}'$  in the modulation speed. Then, using  $\mathbf{r}' \approx \mathbf{r} - \mathbf{v}t$ ,  $\mathbf{V} \approx \begin{pmatrix} 0 & \mathbf{v} \times \mathbf{1} \\ -\mathbf{v} \times \mathbf{1} & 0 \end{pmatrix}$ ,

$\mathbf{A} \approx \mathbf{1}_{6 \times 6}$ , and  $[\mathbf{A} + \mathbf{V} \cdot \mathbf{M}]^{-1} \approx \mathbf{1} - \mathbf{V} \cdot \mathbf{M}$ , it is found that:

$$\mathbf{M}' \approx \mathbf{M} + \left[ \frac{1}{c_0^2} \mathbf{V} - \mathbf{M} \cdot \mathbf{V} \cdot \mathbf{M} \right] = \begin{pmatrix} \boldsymbol{\varepsilon}(\mathbf{r}') & \frac{1}{c_0^2} \mathbf{v} \times \mathbf{1} - \boldsymbol{\varepsilon} \cdot [\mathbf{v} \times \boldsymbol{\mu}] \\ -\frac{1}{c_0^2} \mathbf{v} \times \mathbf{1} + \boldsymbol{\mu} \cdot [\mathbf{v} \times \boldsymbol{\varepsilon}] & \boldsymbol{\mu}(\mathbf{r}') \end{pmatrix}. \quad (\text{S8})$$

Thus, in the non-relativistic limit one obtains:

$$\boldsymbol{\varepsilon}' \approx \boldsymbol{\varepsilon}(\mathbf{r}'), \quad \boldsymbol{\mu}' \approx \boldsymbol{\mu}(\mathbf{r}'), \quad \boldsymbol{\xi}' = \boldsymbol{\zeta}'^T \approx \frac{1}{c_0^2} \mathbf{v} \times \mathbf{1} - \boldsymbol{\varepsilon}(\mathbf{r}') \cdot [\mathbf{v} \times \boldsymbol{\mu}(\mathbf{r}')]. \quad (\text{S9})$$

As seen, the permittivity and permeability are unaffected by the coordinate transformation. Using Eq. (S7) and  $\mathbf{v} = v_x \hat{\mathbf{x}} + v_y \hat{\mathbf{y}}$  one finds that the relevant entries of the magneto-electric tensor can be written explicitly as:

$$\xi'_{zx} \approx -\varepsilon_{zz} \mu_{xy} v_x + \left( \varepsilon_{zz} \mu_{xx} - \frac{1}{c_0^2} \right) v_y, \quad (\text{S10a})$$

$$\xi'_{zy} \approx -\left( \varepsilon_{zz} \mu_{yy} - \frac{1}{c_0^2} \right) v_x + \varepsilon_{zz} \mu_{xy} v_y. \quad (\text{S10b})$$

Note that the magneto-electric parameters depend explicitly on  $c_0$  and thus are gauge dependent, i.e., transformation dependent.

## II. Exact result for $\mathbf{v} = v_y \hat{\mathbf{y}}$

For completeness, we also show the exact formulas for  $\varepsilon'_{zz}$ ,  $\mu'_{xx}$ ,  $\mu'_{yy}$ ,  $\mu'_{xy}$ ,  $\xi'_{zx}$ ,  $\xi'_{zy}$  for a modulation speed along the y-direction  $\mathbf{v} = v_y \hat{\mathbf{y}}$ :

$$\varepsilon'_{zz} = \frac{\varepsilon_{zz} (1 - v^2 / c_0^2)}{1 - \varepsilon_{zz} \mu_{xx} v^2}, \quad (\text{S11a})$$

$$\mu'_{xx} = \frac{\mu_{xx} (1 - v^2 / c_0^2)}{1 - \varepsilon_{zz} \mu_{xx} v^2}, \quad \mu'_{xy} = \sqrt{1 - \frac{v^2}{c_0^2}} \frac{\mu_{xy}}{1 - \varepsilon_{zz} \mu_{xx} v^2}, \quad \mu'_{yy} = \frac{\mu_{yy} - \varepsilon_{zz} (\mu_{xx} \mu_{yy} - \mu_{xy}^2) v^2}{1 - \varepsilon_{zz} \mu_{xx} v^2} \quad (\text{S11b})$$

$$\xi'_{zx} = \left( \varepsilon_{zz} \mu_{xx} - \frac{1}{c_0^2} \right) \frac{v}{1 - \varepsilon_{zz} \mu_{xx} v^2}, \quad \xi'_{zy} = \sqrt{1 - \frac{v^2}{c_0^2}} \varepsilon_{zz} \mu_{xy} \frac{v}{1 - \varepsilon_{zz} \mu_{xx} v^2}. \quad (\text{S11c})$$

It is underlined that the above formulas apply both to a Lorentz transformation ( $c_0 = c$ ) and to a Galilean transformation ( $c_0 = \infty$ ).

## B. Gauge transformations

As discussed in the Sect. A, there is an arbitrariness in the choice of the coordinate transformation. In fact, the parameter  $c_0$  can be taken arbitrarily in the range  $0 < c_0 \leq \infty$ . All the transformations predict the same electrodynamics in the laboratory frame when the corresponding inverse transformation is applied to the fields and to the spacetime coordinates.

Evidently, the state vector in the co-moving frame depends on the parameter  $c_0$ , i.e.,  $\Psi' = \Psi'_{c_0}$  (explicit formulas for the co-moving frame fields can be found in Ref. [S2]). In the following, we prove that in the non-relativistic limit different state vectors  $\Psi'_{c_0}$  are linked by a gauge transformation, such that

$$\Psi'_{c_0} \equiv \Psi'_{c_0} e^{-\frac{\omega'}{c_0^2} i(v_x x' + v_y y')}, \quad (\text{S12})$$

where  $\mathbf{v} = v_x \hat{\mathbf{x}} + v_y \hat{\mathbf{y}}$  is the modulation speed and  $\Psi'_\infty$  is the state vector for the Galilean case ( $c_0 = \infty$ ).

To begin with, we note that the eigenstates  $\Psi'_\infty$  of the operator obtained with a Galilean transformation satisfy:

$$\begin{pmatrix} 0 & -i\partial_{y'} & +i\partial_{x'} \\ -i\partial_{y'} & 0 & 0 \\ +i\partial_{x'} & 0 & 0 \end{pmatrix} \cdot \Psi'_\infty = \omega' \begin{pmatrix} \varepsilon_{zz}(\mathbf{r}') & \xi'_{zx,G}(\mathbf{r}') & \xi'_{zy,G}(\mathbf{r}') \\ \xi'_{zx,G}(\mathbf{r}') & \mu_{xx}(\mathbf{r}') & \mu_{xy}(\mathbf{r}') \\ \xi'_{zy,G}(\mathbf{r}') & \mu_{xy}(\mathbf{r}') & \mu_{yy}(\mathbf{r}') \end{pmatrix} \cdot \Psi'_\infty, \quad (\text{S13})$$

with  $\omega'$  the oscillation eigenfrequency in the Galilean co-moving frame. We combined Eq. (2) of the main text with Eq. (S10) and  $\boldsymbol{\varepsilon}' \approx \boldsymbol{\varepsilon}(\mathbf{r}')$ ,  $\boldsymbol{\mu}' \approx \boldsymbol{\mu}(\mathbf{r}')$ . In the above,  $\xi'_{zx,G} \approx -\varepsilon_{zz} \mu_{xy} v_x + \varepsilon_{zz} \mu_{xx} v_y$  and  $\xi'_{zy,G} \approx -\varepsilon_{zz} \mu_{yy} v_x + \varepsilon_{zz} \mu_{xy} v_y$  are the magneto-electric parameters evaluated with  $c_0 = \infty$ . From here, it is simple to check that  $\Psi'_{c_0}$  defined as in

Eq. (S12) satisfies:

$$\begin{pmatrix} 0 & -i\partial_{y'} & +i\partial_{x'} \\ -i\partial_{y'} & 0 & 0 \\ +i\partial_{x'} & 0 & 0 \end{pmatrix} \cdot \Psi'_{c_0} = \omega' \begin{pmatrix} \varepsilon_{zz}(\mathbf{r}') & \xi'_{zx,G}(\mathbf{r}') - \frac{v_y}{c_0^2} & \xi'_{zy,G}(\mathbf{r}') + \frac{v_x}{c_0^2} \\ \xi'_{zx,G}(\mathbf{r}') - \frac{v_y}{c_0^2} & \mu_{xx}(\mathbf{r}') & \mu_{xy}(\mathbf{r}') \\ \xi'_{zy,G}(\mathbf{r}') + \frac{v_x}{c_0^2} & \mu_{xy}(\mathbf{r}') & \mu_{yy}(\mathbf{r}') \end{pmatrix} \cdot \Psi'_{c_0}. \quad (\text{S14})$$

But since  $\xi'_{zx} = \xi'_{zx,G} - \frac{v_y}{c_0^2}$  and  $\xi'_{zy} = \xi'_{zy,G} + \frac{v_x}{c_0^2}$ , it follows that the eigenstates of the operator constructed with a generalized Lorentz  $c_0$ -transformation are linked to the eigenstates obtained with a Galilean transformation as in Eq. (S12). Thus,  $\Psi'$  can be understood as a gauge field. The gauge degree freedom is associated with the

arbitrariness of the parameter  $c_0$ . It is underlined that even though the eigenstates in the co-moving frame depend on the gauge (i.e., depend on  $c_0$ ), the corresponding fields in the laboratory frame are by construction gauge independent.

### C. Synthetic magnetic potential

#### I. Non-relativistic limit

As shown in Refs. [S4-S6] based on an analogy with the Schrödinger equation, the bianisotropic coupling determines a synthetic magnetic potential. For TE-polarized waves, it is given by  $\mathbf{A} = [c\xi'_{zx}\hat{\mathbf{x}} + c\xi'_{zy}\hat{\mathbf{y}}] \times \hat{\mathbf{z}}$  (see Appendix B of Ref. [S6]).

For simplicity, in the following discussion we focus on the nonrelativistic limit. In such a case,  $\xi'_{zx}$ ,  $\xi'_{zy}$  can be evaluated using Eq. (S10). Hence, the magnetic potential reduces to:

$$\frac{\mathbf{A}}{c} \approx \left[ -\left( \varepsilon_{zz}\mu_{yy} - \frac{1}{c_0^2} \right) v_x + \varepsilon_{zz}\mu_{xy} v_y \right] \hat{\mathbf{x}} + \left[ \varepsilon_{zz}\mu_{xy} v_x - \left( \varepsilon_{zz}\mu_{xx} - \frac{1}{c_0^2} \right) v_y \right] \hat{\mathbf{y}}. \quad (\text{S15})$$

In the particular case of an isotropic material,  $\mu \equiv \mu_{xx} = \mu_{yy}$ ,  $\mu_{xy} = 0$ ,  $\varepsilon \equiv \varepsilon_{zz}$  the vector potential can be written as  $\mathbf{A} \approx -(n^2 - c^2 / c_0^2) \mathbf{v} / c$  with  $n = c\sqrt{\varepsilon\mu}$  the refractive index of the material. Thus, in the isotropic case the direction of the vector potential is locked to the direction of the modulation speed. Note that for a Lorentz transformation ( $c_0 = c$ ) the magnetic potential reduces to  $\mathbf{A} \approx -(n^2 - 1) \mathbf{v} / c$  which is the result discussed in the main text.

#### II. Perturbation of an isorefractive crystal

Consider now an isotropic spacetime crystal ( $\mu \equiv \mu_{xx} = \mu_{yy}$ ,  $\mu_{xy} = 0$ ,  $\varepsilon \equiv \varepsilon_{zz}$ ) formed by isorefractive materials so that  $n = c\sqrt{\varepsilon\mu} = \text{const.}$ . Then, there is a gauge for which the magneto-electric coefficients  $\xi'_{zx}$ ,  $\xi'_{zy}$  vanish exactly [S2]. Specifically, the relevant gauge is associated with the generalized Lorentz transformation with  $c_0 = c/n$  [see Eq. (S11c)]. This result is exact, i.e., it does not require a linear  $v$  approximation. Isorefractive media with  $n = \text{const.}$  are “fixed points” of the generalized  $c_0 = c/n$  Lorentz transformation, in the sense that they stay invariant under the coordinate transformation. In particular, it was recently shown that spacetime crystals formed by materials with  $n = 1$  behave exactly as moving photonic crystals [S2]. Such crystals are designated by Minkowskian spacetime crystals.

It is evident that any isorefractive spacetime crystal must be topologically trivial. In fact, the crystal response in a suitable co-moving frame ( $c_0 = c/n$ ) is reciprocal ( $\xi'_{zx} = 0 = \xi'_{zy}$ ). Furthermore, the synthetic magnetic potential vanishes in the generalized Lorentz  $c_0 = c/n$  co-moving frame. For a generic coordinate transformation,  $\mathbf{A} \approx (n^2 - c^2/c_0^2)\mathbf{v}/c = \text{const.}$ , which corresponds to a trivial synthetic magnetic field ( $\nabla \times \mathbf{A} = 0$ ), in agreement with the trivial topology.

It is interesting to study how the magnetic potential changes if one perturbs slightly an isorefractive spacetime crystal. To investigate this, we assume that the magnetic response may be slightly anisotropic so that the in-plane permeability is of the form:

$$\boldsymbol{\mu}_{\text{in-plane}}(\mathbf{r}, t) = \mu \left[ (1 + \delta_\mu) \hat{\mathbf{e}}_1 \otimes \hat{\mathbf{e}}_1 + (1 - \delta_\mu) \hat{\mathbf{e}}_2 \otimes \hat{\mathbf{e}}_2 \right]. \quad (\text{S16})$$

Here,  $\hat{\mathbf{e}}_1, \hat{\mathbf{e}}_2$  are the in-plane orthogonal permeability main axes, defined so that  $\hat{\mathbf{e}}_1 \times \hat{\mathbf{e}}_2 = \hat{\mathbf{z}}$ . The in-plane permeability eigenvalues are  $\mu(1 \pm \delta_\mu)$ . All the parameters ( $\hat{\mathbf{e}}_1, \hat{\mathbf{e}}_2, \mu, \delta_\mu$ ) are functions of  $\mathbf{r} - \mathbf{v}t$  in the laboratory frame coordinates. Furthermore, it is supposed that  $\varepsilon_{zz}\mu = \text{const.} \equiv n^2 / c^2$  so that when  $\delta_\mu = 0$  the crystal is isorefractive. Thus,  $\delta_\mu$  represents the detuning with respect to the isorefractive condition.

Let us denote  $\hat{\mathbf{e}}_1 = \cos(\varphi_\mu)\hat{\mathbf{x}} + \sin(\varphi_\mu)\hat{\mathbf{y}}$ ,  $\hat{\mathbf{e}}_2 = -\sin(\varphi_\mu)\hat{\mathbf{x}} + \cos(\varphi_\mu)\hat{\mathbf{y}}$ , so that  $\varphi_\mu$  represents the angle of the main axis  $\hat{\mathbf{e}}_1$  with respect to the  $x$ -direction (see Fig. 2a).

Then, we have:

$$\mu_{xx} = \mu(1 + \delta_\mu)\cos^2(\varphi_\mu) + \mu(1 - \delta_\mu)\sin^2(\varphi_\mu) = \mu[1 + \delta_\mu \cos(2\varphi_\mu)], \quad (\text{S17a})$$

$$\mu_{yy} = \mu(1 + \delta_\mu)\sin^2(\varphi_\mu) + \mu(1 - \delta_\mu)\cos^2(\varphi_\mu) = \mu[1 - \delta_\mu \cos(2\varphi_\mu)]. \quad (\text{S17b})$$

$$\mu_{xy} = 2\mu\delta_\mu \cos(\varphi_\mu)\sin(\varphi_\mu) = \mu\delta_\mu \sin(2\varphi_\mu). \quad (\text{S17c})$$

Let us also write  $\mathbf{v} = v[\cos(\varphi_v)\hat{\mathbf{x}} + \sin(\varphi_v)\hat{\mathbf{y}}]$  so that  $\varphi_v$  represents the angle of the modulation speed  $\mathbf{v}$  with respect to the  $x$ -direction (see Fig. 2a). Substituting these formulas in Eq. (S15), one finds that the synthetic magnetic potential is:

$$\mathbf{A} \approx -\frac{\mathbf{v}}{c} \left( n^2 - \frac{c^2}{c_0^2} \right) + n^2 \frac{v}{c} \delta_\mu \hat{\mathbf{e}}_A. \quad (\text{S18})$$

The first term on the right-hand side is the constant synthetic potential for the isorefractive crystal, which has no impact on the topology. The interesting piece is the second term. Its direction is ruled by the relative orientation of the main axes of the permeability with respect to the modulation speed:



$\hat{\mathbf{e}}_A \equiv \cos(2\varphi_\mu - \varphi_\nu)\hat{\mathbf{x}} + \sin(2\varphi_\mu - \varphi_\nu)\hat{\mathbf{y}}$ . In particular, if we pick the gauge  $c_0 = c/n$  the magnetic potential becomes  $\mathbf{A} \approx n^2 \frac{v}{c} \delta_\mu \hat{\mathbf{e}}_A$ . In the main text, we construct a spacetime crystal that corresponds to the perturbation of a Minkowskian crystal with  $n=1$ . In this case, the vector potential reduces to  $\mathbf{A} \approx \frac{v}{c} \delta_\mu \hat{\mathbf{e}}_A$  in the Lorentz co-moving frame.

#### D. Band structure of the spacetime crystal

The electromagnetic modes in the co-moving frame coordinates are regular Bloch waves. This is so because the material matrix  $\mathbf{M}'_{\text{TE}}$  is periodic in the primed coordinates. From Eq. (2), the TE Bloch waves with envelope  $\Psi_{\mathbf{p}}$  are solutions of the generalized eigenvalue problem:

$$\underbrace{\begin{pmatrix} 0 & -i\partial_{y'} + k'_y & +i\partial_{x'} - k'_x \\ -i\partial_{y'} + k'_y & 0 & 0 \\ +i\partial_{x'} - k'_x & 0 & 0 \end{pmatrix}}_{\mathbf{L}_{\mathbf{k}'}} \cdot \Psi_{\mathbf{p}} = \omega' \underbrace{\begin{pmatrix} \epsilon'_{zz} & \xi'_{zx} & \xi'_{zy} \\ \xi'_{zx} & \mu'_{xx} & \mu'_{xy} \\ \xi'_{zy} & \mu'_{xy} & \mu'_{yy} \end{pmatrix}}_{\mathbf{M}'_{\text{TE}}} \cdot \Psi_{\mathbf{p}}. \quad (\text{S19})$$

Here,  $\mathbf{k}' = k'_x \hat{\mathbf{x}} + k'_y \hat{\mathbf{y}}$  is the wave vector of the Bloch wave and  $\omega'$  is the frequency.

The band structure in the co-moving frame coordinates can be found using a plane wave expansion:

$$\Psi_{\mathbf{p}}(\mathbf{r}') = \sum_{\mathbf{q} \in \mathbb{Z}^2} \psi_{\mathbf{q}} e^{i\mathbf{G}_{\mathbf{q}}^0 \cdot \mathbf{r}'} \psi_{\mathbf{q}} = \begin{pmatrix} \psi_{1,\mathbf{q}} \\ \psi_{1,\mathbf{q}} \\ \psi_{1,\mathbf{q}} \end{pmatrix}. \quad (\text{S20})$$

where  $\mathbf{G}_{\mathbf{q}}^0 = q_1 \mathbf{b}'_1 + q_2 \mathbf{b}'_2$  is a generic vector of the reciprocal lattice. The primitive vectors of the reciprocal and direct lattices are related in the usual manner  $\mathbf{b}'_i \cdot \mathbf{a}'_j = 2\pi \delta_{ij}$ .

Furthermore, since the material matrix is a periodic function, it can also be expanded into plane waves as:

$$\mathbf{M}'_{\text{TE}}(\mathbf{r}') = \sum_{\mathbf{q} \in \mathbb{Z}^2} \mathbf{M}'_{\mathbf{q}} e^{i\mathbf{G}_{\mathbf{q}}^0 \cdot \mathbf{r}'}, \quad \text{with} \quad \mathbf{M}'_{\mathbf{q}} = \begin{pmatrix} \varepsilon'_{zz,\mathbf{q}} & \xi'_{zx,\mathbf{q}} & \xi'_{zy,\mathbf{q}} \\ \xi'_{zx,\mathbf{q}} & \mu'_{xx,\mathbf{q}} & \mu'_{xy,\mathbf{q}} \\ \xi'_{zy,\mathbf{q}} & \mu'_{xy,\mathbf{q}} & \mu'_{yy,\mathbf{q}} \end{pmatrix}. \quad (\text{S21})$$

When the material inclusions have a circular cross-section (as in the main text), the Fourier coefficients  $\mathbf{M}_{\mathbf{q}}$  can be expressed in terms of cylindrical Bessel functions, similar to Refs. [S5, S6, S7] (not shown). Substituting the previous formulas into Eq. (S19), one obtains a generalized matrix eigenvalue problem:

$$\begin{pmatrix} [0] & [\mathbf{G}_{\mathbf{p}} \cdot \hat{\mathbf{y}} \delta_{\mathbf{p}-\mathbf{q}}] & [-\mathbf{G}_{\mathbf{p}} \cdot \hat{\mathbf{x}} \delta_{\mathbf{p}-\mathbf{q}}] \\ [\mathbf{G}_{\mathbf{p}} \cdot \hat{\mathbf{y}} \delta_{\mathbf{p}-\mathbf{q}}] & [0] & [0] \\ [-\mathbf{G}_{\mathbf{p}} \cdot \hat{\mathbf{x}} \delta_{\mathbf{p}-\mathbf{q}}] & [0] & [0] \end{pmatrix} \cdot \begin{pmatrix} (\psi_{1,\mathbf{q}}) \\ (\psi_{2,\mathbf{q}}) \\ (\psi_{3,\mathbf{q}}) \end{pmatrix} = \omega' \begin{pmatrix} [\varepsilon'_{zz,\mathbf{p}-\mathbf{q}}] & [\xi'_{zx,\mathbf{p}-\mathbf{q}}] & [\xi'_{zy,\mathbf{p}-\mathbf{q}}] \\ [\xi'_{zx,\mathbf{p}-\mathbf{q}}] & [\mu'_{xx,\mathbf{p}-\mathbf{q}}] & [\mu'_{xy,\mathbf{p}-\mathbf{q}}] \\ [\xi'_{zy,\mathbf{p}-\mathbf{q}}] & [\mu'_{xy,\mathbf{p}-\mathbf{q}}] & [\mu'_{yy,\mathbf{p}-\mathbf{q}}] \end{pmatrix} \cdot \begin{pmatrix} (\psi_{1,\mathbf{q}}) \\ (\psi_{2,\mathbf{q}}) \\ (\psi_{3,\mathbf{q}}) \end{pmatrix} \quad (\text{S22})$$

with  $\mathbf{G}_{\mathbf{q}} = \mathbf{k}' + \mathbf{G}_{\mathbf{q}}^0$  and  $\mathbf{p}, \mathbf{q} \in \mathbb{Z}^2$ . The sub-blocks  $[A_{\mathbf{p},\mathbf{q}}]$  and  $(F_{\mathbf{q}})$  represent square matrices and vectors, respectively, with infinite dimension. In practice, the plane wave expansion is truncated so that all the matrices have a finite rank. It can be shown that the material matrix is positive definite in the subluminal regime, i.e., when the modulation speed is smaller than the speed of light in the considered materials (as in all the examples of this work). Thus, the generalized eigenvalue problem can be reduced to a standard matrix eigensystem using a Cholesky decomposition of the material matrix.

### ***E. Calculation of the gap Chern number***

The topological charge of the spacetime crystal is calculated in the co-moving frame coordinates. In the co-moving frame, the spectral problem reduces to a standard

eigensystem as shown in Eq. (S19). The solutions are Bloch waves defined in the Brillouin zone (BZ) of the reciprocal space. The Berry curvature can be calculated from the Green's function of the system [S5, S6, S7] defined as:

$$\mathbf{G}_{\mathbf{k}'}(\omega') = i(\mathbf{L}_{\mathbf{k}'} - \omega' \mathbf{M}'_{\text{TE}})^{-1}, \quad (\text{S23})$$

with the operators  $\mathbf{L}_{\mathbf{k}'}$ ,  $\mathbf{M}'_{\text{TE}}$  determined by Eq. (S19). At a given point  $\mathbf{k}' \in \text{BZ}$ , the Berry curvature is found by integrating the Green's function in the complex frequency plane [S5, S6, S7]:

$$\mathcal{F}_{\mathbf{k}'} = \frac{i}{(2\pi)^2} \int_{\omega'_{\text{gap}} - i\infty}^{\omega'_{\text{gap}} + i\infty} d\omega' \text{Tr} \left\{ \frac{\partial \mathbf{L}_{\mathbf{k}'}}{\partial k'_x} \cdot \mathbf{G}_{\mathbf{k}'}(\omega') \cdot \frac{\partial \mathbf{L}_{\mathbf{k}'}}{\partial k'_y} \cdot \mathbf{G}_{\mathbf{k}'}(\omega') \cdot \mathbf{M}'_{\text{TE}} \cdot \mathbf{G}_{\mathbf{k}'}(\omega') \right\}. \quad (\text{S24})$$

The integration path is the line  $\text{Re}\{\omega'\} = \omega'_{\text{gap}}$  parallel to the imaginary frequency axis, with  $\omega'_{\text{gap}}$  some frequency in the relevant band gap. The gap Chern number is found by integrating the Berry curvature over the Brillouin zone:

$$\mathcal{C}_{\text{gap}} = \iint_{\text{BZ}} \mathcal{F}_{\mathbf{k}'} d^2 \mathbf{k}'. \quad (\text{S25})$$

In the numerical calculations, all the operators are represented by the matrices obtained with the plane wave expansion.

The topological charge is independent of the coordinate transformation (independent of  $c_0$ ) because the eigenfunctions associated with different generalized Lorentz transformations are linked as  $\Psi' \rightarrow \Psi' e^{i\mathbf{k}_\Delta \cdot \mathbf{r}'}$  with  $\mathbf{k}_\Delta$  some vector independent of  $\mathbf{r}'$  (see the supplementary note B).

Figure S1a shows a density plot of the Berry curvature [Eq. (S24)] for the band gap highlighted in Fig. 3b of the main text. We integrate Eq. (S24) using

$\mathcal{F}_{\mathbf{k}'} = \frac{-1}{(2\pi)^2} \int_{-\infty}^{+\infty} d\xi \text{Tr}\{\dots\}_{\omega'=\omega'_{\text{gap}}+i\xi}$ . The integration is performed numerically using the

trapezoidal rule. The integrand is discretized into  $N_\xi$  sampling points and the integration range is truncated to an interval of the type  $-\xi_{\text{max}} < \xi < \xi_{\text{max}}$ . As seen, the Berry curvature is strongly concentrated near two points of the reciprocal space, which coincide approximately with the Dirac points. Note that in Fig. S1 we parameterize the Brillouin zone using  $\mathbf{k}' = \beta_1 \mathbf{b}'_1 + \beta_2 \mathbf{b}'_2$  with  $|\beta_i| < 1/2$ .

Furthermore, the gap Chern number is numerically evaluated using

$$\mathcal{C}_{\text{gap}} = \int_{-1/2}^{1/2} d\beta_1 \int_{-1/2}^{1/2} d\beta_2 \mathcal{F}_{\mathbf{k}'=\beta_1 \mathbf{b}'_1 + \beta_2 \mathbf{b}'_2} |\mathbf{b}'_1 \times \mathbf{b}'_2|$$
 with the Brillouin Zone discretized into  $N_x \times N_y$

points. Figure S1b shows the convergence of the numerically calculated gap Chern number as a function of  $N_x = N_y$  for  $\xi_{\text{max}} = 0.1c/a$  and  $N_\xi = 100$ , confirming that for sufficiently large  $N_x = N_y$  the gap Chern number approaches an integer. We performed similar convergence tests in  $\xi_{\text{max}}$  and  $N_\xi$ .

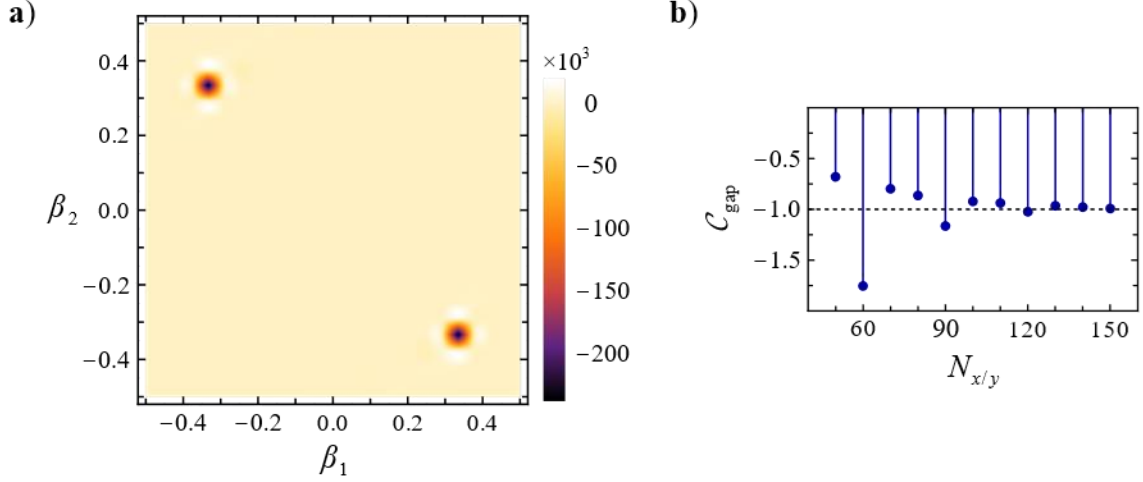


**Fig. S1 a)** Normalized Berry curvature  $|\mathbf{b}'_1 \times \mathbf{b}'_2| \cdot \mathcal{F}_{\mathbf{k}'}$  with  $\mathbf{k}' = \beta_1 \mathbf{b}'_1 + \beta_2 \mathbf{b}'_2$  for the band gap shaded in blue in Fig. 3b of the main text. **b)** Gap Chern number convergence analysis as a function of the number of points  $N_{x/y}$  used to discretize each direction of the Brillouin Zone.

## F. Symmetry constraints on the emergence of unidirectional edge modes

In this supplementary note, we discuss how some discrete symmetries constraint the formation of topological states.

It is well known that a system that possesses either a time-reversal symmetry ( $\mathcal{T}$ ), or a mirror symmetry (e.g., a mirror symmetry with respect to the  $x$ -direction  $\mathcal{P}_x: (x, y) \rightarrow (-x, y)$ ) or a parity-time symmetry ( $\mathcal{P} \cdot \mathcal{T}$ , with  $\mathcal{P}: (x, y) \rightarrow (-x, -y)$  corresponding to a two-fold rotation) is necessarily topologically trivial. Formally, this happens because the Berry curvature has an odd symmetry in the Brillouin Zone and, consequently, the gap Chern number is trivial. For example, for a  $\mathcal{P}_x$ -symmetric system, the Berry curvature satisfies  $\mathcal{F}_{(k_x, k_y)} = -\mathcal{F}_{(-k_x, k_y)}$  and hence its integral over the Brillouin zone vanishes.

It is interesting to justify these properties in a more geometrical way. To this end, in the following we discuss how a given symmetry constraints the net number of unidirectional edge modes at an interface with a trivial topological insulator (e.g., a perfectly electric conducting, PEC, wall). This approach based on the bulk-edge correspondence provides a simple and intuitive method to grasp how different symmetries may constraint the design of non-trivial topologies.

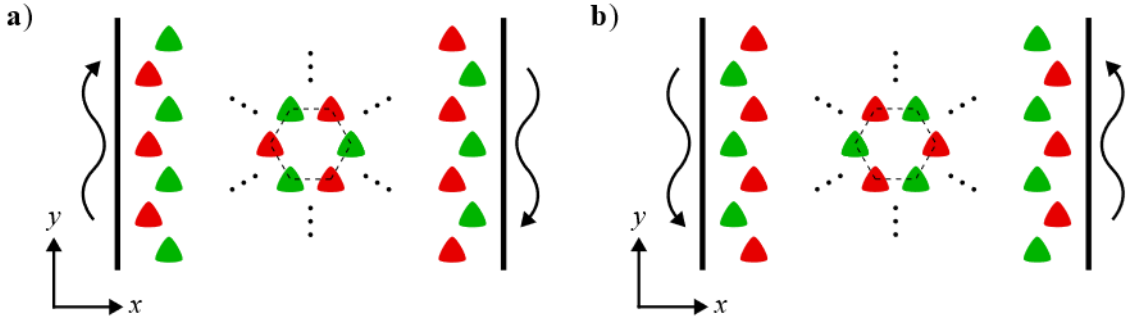


**Fig. S2 a)** Illustration of a photonic crystal with a honeycomb lattice structure enclosed in a cavity with PEC walls (represented in black). The black arrows represent the propagation of an edge mode in the clockwise direction around the cavity walls. The unit cell of the unbounded crystal is formed by two inequivalent elements represented in green and red colors. **b)** Photonic crystal in a) after the action of the mirror operator  $\mathcal{P}_x$ : the red elements switch position with the green elements and the edge mode propagates in the counterclockwise direction.

Let us take the mirror symmetry  $\mathcal{P}_x$  as an example. Figure S2a represents a photonic crystal with a honeycomb structure enclosed in a large metallic cavity with PEC walls. From the bulk-edge correspondence, the net number of unidirectional states circulating in the counterclockwise direction around the cavity is identical to  $-\mathcal{C}_{\text{gap}}$ , with  $\mathcal{C}_{\text{gap}}$  the topological charge of the band gap [S8]. The unit cell of the unbounded crystal is formed by two inequivalent elements depicted in green and red in Fig. S2.

Under the  $\mathcal{P}_x$  mirror operation, the considered photonic crystal is transformed into a new crystal where the positions of the red and green elements are interchanged (Fig. S2b). Furthermore, under the  $\mathcal{P}_x$  operation, all the edge modes propagating in the counterclockwise (clockwise) direction are transformed into modes circulating in the clockwise (counterclockwise) direction. This property implies that the gap Chern number of the  $\mathcal{P}_x$ -transformed system has the opposite sign as the gap Chern number of the original system. In particular, when the system is  $\mathcal{P}_x$ -invariant, the gap Chern number must be exactly zero, and thereby such systems cannot support unidirectional edge modes. The same analysis can be done for other symmetries.

It is interesting to analyze in further detail how the mirror symmetry constraints the formation of nontrivial topologies in spacetime crystals. To this end, we consider again a crystal with a honeycomb lattice but now subject to a spacetime modulation with the modulation velocity directed along the  $y$ -direction (Fig. S3). As before, the crystal is enclosed in a cavity with opaque walls. If the red and green elements are different, the crystal breaks simultaneously the  $\mathcal{T}$  and  $\mathcal{P}\cdot\mathcal{T}$  symmetries.

Let us focus on the mirror symmetry  $\mathcal{P}_x:(x, y) \rightarrow (-x, y)$ , so that the modulation velocity ( $\mathbf{v} = v\hat{\mathbf{y}}$ ) is parallel to the mirror. Under the action of  $\mathcal{P}_x$ , the system of Fig. S3a is transformed into the system of Fig. S3b. As seen, the  $\mathcal{P}_x$  mirror operator preserves the modulation speed but flips the direction of circulation of all the edge modes. In particular, it follows that to have a nontrivial topology the unit cell cannot have  $\mathcal{P}_x$ -mirror symmetry. The mirror symmetry can be broken with scatterers with a triangular shape, as

shown in Fig. S3. This example clearly shows that a nontrivial topology requires a unit cell without any mirror-plane parallel to the modulation velocity. In contrast, mirrors perpendicular to the direction of the modulation speed do not constraint the topological charge of the spacetime crystal.

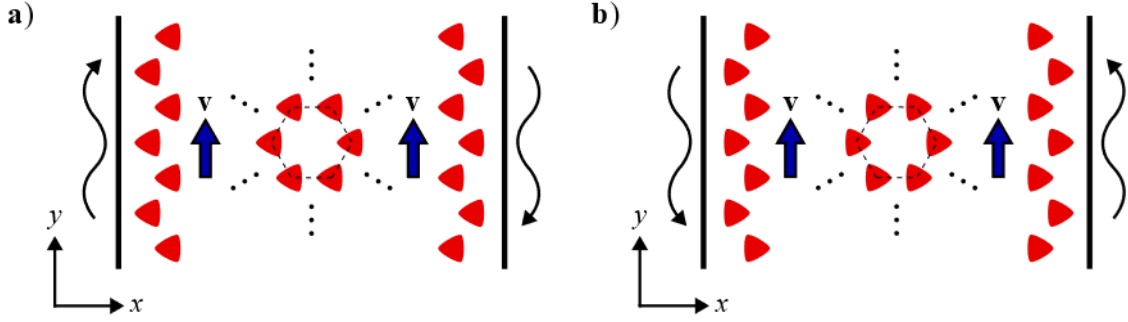


**Fig. S3** **a)** Similar to Fig. S2a but for a spacetime crystal with a traveling-wave modulation with velocity  $\mathbf{v} = v\hat{y}$ . **b)** Photonic crystal in a) after the action of the mirror symmetry operator  $\mathcal{P}_x$ : the modulation velocity is preserved, but the direction of propagation of the edge modes is flipped. To generate non-trivial topologies, the unit cell must have a broken  $\mathcal{P}_x$ -symmetry (as in the figure).

### *G. Spacetime crystals with a square lattice*

In this supplementary note, we study the band structure and topology of a spacetime crystal with dielectric elements organized in a square lattice (Fig. S4a). The modulation velocity is along the  $y$ -direction.

From the supplementary note F, a nontrivial topology is possible only if the unit cell does not have any mirror-plane parallel to  $\mathbf{v} = v\hat{y}$ . To ensure this, the dielectric scatterers have a diamond-shape cross-section with a lateral “cut” (red structures in Fig. S4a). In Ref. [S9], it was shown that a square lattice may exhibit two pairs of Dirac cones, one protected by the  $\mathcal{P}_x$  symmetry and the other one by the  $\mathcal{P}_y$  symmetry. Since the geometry



of our inclusions breaks the  $\mathcal{P}_x$  symmetry, the photonic band structure in the static case ( $v=0$ ) presents only one pair of Dirac cones over the high-symmetry lines  $Y-M$  protected by the  $\mathcal{P}_y$  symmetry (Fig. S4b). When the spacetime modulation is switched on ( $v \neq 0$ ), the Dirac degeneracies are lifted and a complete band gap is formed (Fig. S4c). However, it turns out that the band gap is topologically trivial ( $\mathcal{C}_{\text{gap}} = 0$ ), similar to the example in Fig. 1 of the main text. Figure S4d shows that the topological charge density is concentrated at the two Dirac points on the high-symmetry lines  $X-M$  ( $\beta_1 = \pm 0.5$ ). The topological charge density has an opposite sign at each Dirac point, hence the trivial Chern topology. Thus, a broken  $\mathcal{P}_x$ -mirror symmetry and a broken 2-fold rotation symmetry do not guarantee the emergence of nontrivial topological phases.

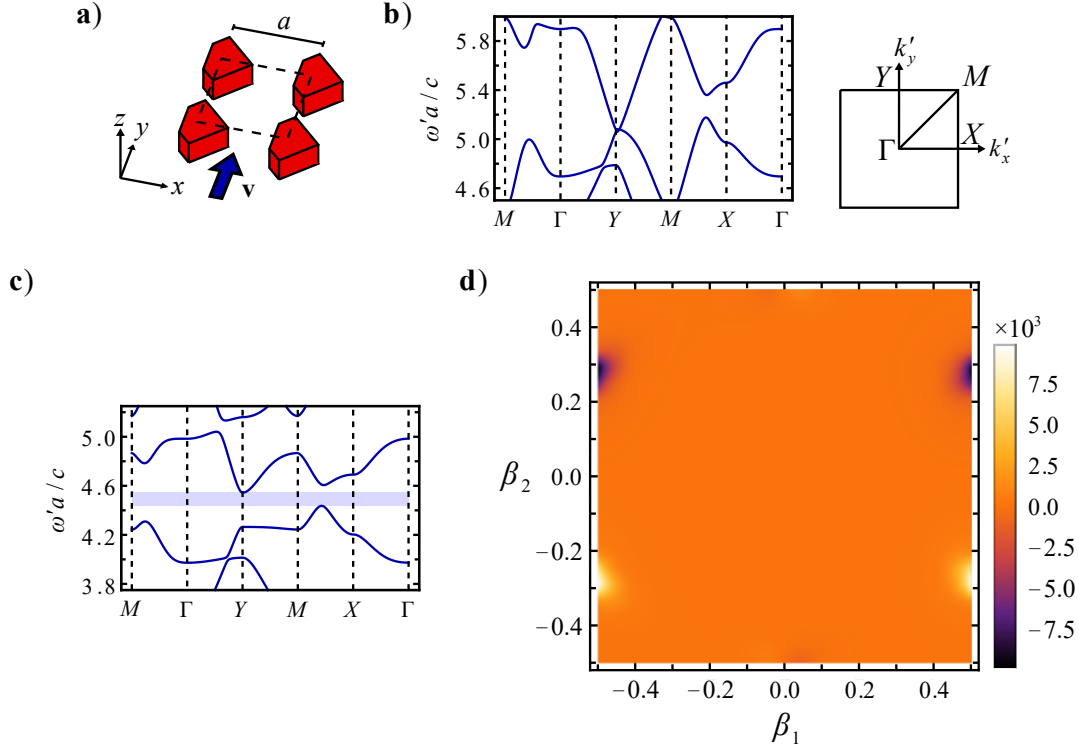


**Fig. S4** **a)** Unit cell of a spacetime crystal with the dielectric scatterers organized in a square lattice in the Lorentz co-moving frame. The modulation velocity is  $\mathbf{v} = v\hat{\mathbf{y}}$ . The dielectric inclusion ( $\epsilon = 8\epsilon_0$ ,  $\mu = \mu_0$ ) has a diamond-like geometry with a lateral cut that breaks the  $\mathcal{P}_x$  symmetry. **b)** (Left) Band structure in the Lorentz co-moving frame for  $v=0$ . (Right) Brillouin Zone in the dual space of the Lorentz co-moving frame. **c)** Band structure for  $v=0.2c$ . The band gap corresponding to the horizontal blue strip is characterized by  $\mathcal{C}_{\text{gap}} = 0$ . **d)** Normalized Berry curvature  $|\mathbf{b}'_1 \times \mathbf{b}'_2| \mathcal{F}_{\mathbf{k}}$ , with  $\mathbf{k}' = \beta_1 \mathbf{b}'_1 + \beta_2 \mathbf{b}'_2$  for the band gap shaded in blue in c).

## H. Other implementations of the “anisotropic ring”

In this supplementary note, we discuss different approximations of the anisotropic ring introduced in the main text (see Fig. 2bi). Similar to the main text, the continuous ring is approximated by an array of discrete scatterers.

We start with the simplest and crudest approximation of the ring, using only  $N=2$  scatterers (bluish elements in Fig. S5a). Similar to the main text, the “ring” perturbs slightly a Minkowskian isorefractive crystal with  $n=1$  corresponding to the red elements embedded in vacuum. The modulation velocity is along  $y$  ( $\mathbf{v} = v\hat{\mathbf{y}}$ ).

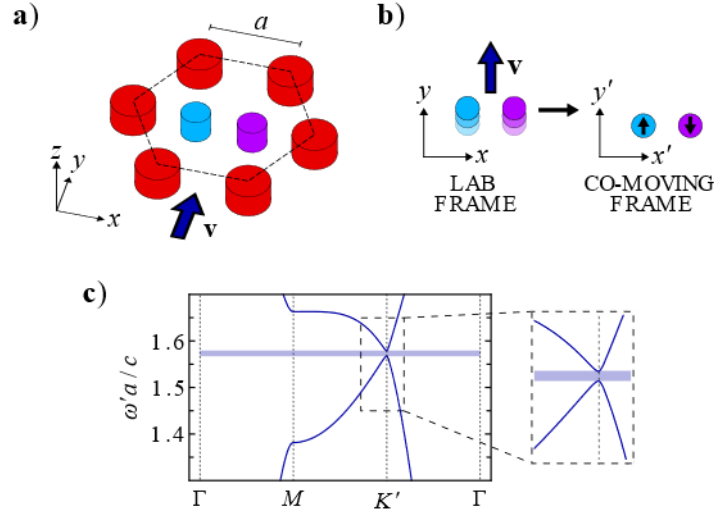


**Fig. S5 a)** Unit cell of a honeycomb array of scatterers (red elements with radius  $R_r = 0.2a$ ) with the same refractive index as the vacuum background:  $\epsilon = 10\epsilon_0$ ,  $\mu = 0.1\mu_0$ . The isorefractive structure is perturbed with two additional elements of radius  $R_b = 0.25a$  (bluish colors) with parameters  $\epsilon = \epsilon_0$ ,  $\mu = 1.5\mu_0$  (light blue element) and  $\epsilon = \epsilon_0$ ,  $\mu = 0.5\mu_0$  (dark blue element). The modulation velocity is  $\mathbf{v} = v\hat{\mathbf{y}}$ ; in the lab frame, the crystal is Lorentz contracted. **b)** Synthetic magnetic potential  $\mathbf{A}$  (black arrows) in the Lorentz co-moving frame implemented by the blue isotropic elements. **c)** Band structure in the Lorentz co-moving frame for a modulation speed  $v = 0.3c$ . The topological charge is  $\mathcal{C}_{\text{gap}} = -1$ .

Interestingly, the “ring” with two scatterers can be implemented using only isotropic materials. In fact, the vector potential in the isotropic case reduces to  $\mathbf{A} \approx -(n^2 - 1)\mathbf{v}/c$  and hence it is possible to engineer the *orientation*  $\pm\hat{\mathbf{y}}$  simply using materials with a refractive index greater and smaller than the background material (see Fig. S5b). To this

end, we use scatterers with the material parameters  $\varepsilon = \varepsilon_0$ ,  $\mu = (1 \pm 0.5)\mu_0$  (bluish elements in Fig. S5a). Similar to the main text, as the red elements and the background are isorefractive, only the blue scatterers contribute to the synthetic magnetic potential. Figure S5c depicts the band structure in the Lorentz co-moving frame for  $v = 0.3c$ . The blue elements are separated by  $0.6a$ . A detailed analysis shows that the band gap shaded in blue has topological charge  $\mathcal{C}_{\text{gap}} = -1$ , in agreement with the more complex ring with  $N = 3$  elements considered in the main text.

The band gap obtained with the  $N = 2$  ring is rather narrow and hence it is more sensitive to perturbations. It is possible to engineer more robust topological phases by considering better approximations of the anisotropic ring. This is illustrated in the final example (Fig. S6) which considers an approximation of the ring using  $N = 6$  elements. Now, each element of the ring is an anisotropic material with the permeability main axes controlled by  $\varphi_{\mu,n} = \frac{\pi}{2} + \frac{\varphi_n}{2}$  with  $\varphi_n = -\frac{\pi}{2} + (n-1)\frac{2\pi}{6}$  and  $n = 1, \dots, 6$ . Here, we use circular scatterers merely to simplify the numerical modelling.

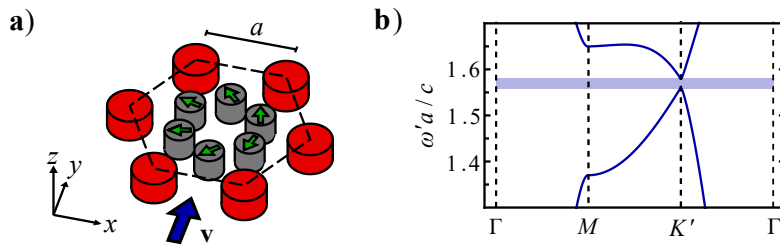


**Fig. S6 a)** Unit cell of a spacetime crystal constructed from an isorefractive system (air background plus the honeycomb array of isotropic red elements with  $\varepsilon = 10\varepsilon_0$  and  $\mu = 0.1\mu_0$ ) perturbed with the gray anisotropic elements. The elements in gray provide a discrete realization of the anisotropic ring (Fig. 2bi) with six elements. They have an anisotropic response characterized by the detuning parameter  $\delta_\mu = 0.5$

and the permeability main axes  $\hat{\mathbf{e}}_1$  are represented by the green arrows. The red and gray elements have circular cross-sections with radii  $R_r = 0.2a$  and  $R_g = 0.17a$ , respectively. All the dimensions are specified in the Lorentz co-moving frame. **c)** Band structure in the Lorentz co-moving frame for a modulation speed  $v = 0.2c$  along the  $y$ -direction. The band gap is characterized by  $\mathcal{C}_{\text{gap}} = -1$ .

Figure S6 confirms that the band gap of the crystal based on the  $N = 6$  approximation of the anisotropic ring is approximately 35% wider than the gap obtained with the  $N = 3$  approximation. As expected, the topological charge of the band gap remains  $\mathcal{C}_{\text{gap}} = -1$ , confirming that the topology does not change with  $N$ . The topological band diagram is qualitatively similar to that in Fig. 3 of the main text (not shown here).

### Supplemental Material References:

- [S1] F. R. Prudêncio, M. G. Silveirinha, “Synthetic Axion Response with Spacetime Crystals”, *Phys. Rev. Appl.*, **19**, 024031, 2023.
- [S2] F. R. Prudêncio, M. G. Silveirinha, “Replicating Physical Motion with Minkowskian Isorefractive Spacetime Crystals”, *Nanophotonics*, doi.org/10.1515/nanoph-2023-0144 (2023).
- [S3] P. A. Huidobro, M. G. Silveirinha, E. Galiffi, J. B. Pendry, “Homogenization Theory of Space-Time Metamaterials”, *Phys. Rev. Appl.* **16**, 014044 (2021).
- [S4] S. Lannebère, M. G. Silveirinha, “Photonic analogues of the Haldane and Kane-Mele models”, *Nanophotonics* **8**, 1387 (2019).
- [S5] F. R. Prudêncio, M. G. Silveirinha, “First principles calculation of the topological phases of the photonic Haldane model”, *Symmetry* **13**, 2229 (2021).
- [S6] J. C. Serra, M. G. Silveirinha, “Rotating spacetime modulation: Topological phases and spacetime Haldane model”, *Phys. Rev. B* **107**, 035133 (2023).
- [S7] F. R. Prudêncio, M. G. Silveirinha, “First principles calculation of topological invariants of non-Hermitian photonic crystals”, *Commun. Phys.* **3**, 221 (2020).
- [S8] M. G. Silveirinha, “Proof of the Bulk-Edge Correspondence through a Link between Topological Photonics and Fluctuation-Electrodynamics”, *Phys. Rev. X* **9**, 011037 (2019).
- [S9] W.-Y. He, C. T. Chan, “The Emergence of Dirac points in Photonic Crystals with Mirror Symmetry”, *Sci. Rep.* **5**, 8186 (2015).